

UCLA

UCLA Previously Published Works

Title

Respiratory motion prediction and prospective correction for free-breathing arterial spin-labeled perfusion MRI of the kidneys

Permalink

<https://escholarship.org/uc/item/5sp2x7xf>

Journal

Medical Physics, 44(3)

ISSN

0094-2405

Authors

Song, Hao
Ruan, Dan
Liu, Wenyang
et al.

Publication Date

2017-03-01

DOI

10.1002/mp.12099

Peer reviewed

Respiratory motion prediction and prospective correction for free-breathing arterial spin-labeled perfusion MRI of the kidneys

Hao Song

Department of Imaging Physics, The University of Texas MD Anderson Cancer Center, Houston, TX 77030, USA

Dan Ruan and Wenyang Liu

Departments of Radiation Oncology, Biomedical Physics and Bioengineering, UCLA, Los Angeles, CA 90095, USA

V. Andrew Stenger

Department of Medicine, University of Hawai'i at Manoa, Honolulu, HI 96813, USA

Rolf Pohmann

High-Field Magnetic Resonance Center, Max Planck Institute for Biological Cybernetics, 72076 Tubingen, Germany

Maria A. Fernández-Seara

Department of Radiology, University of Navarra Hospital, 31008 Pamplona, Spain

Tejas Nair

DMC R&D Center, Samsung Electronics Inc., Seocho-gu, 06765 Seoul, Korea

Sungkyu Jung

Department of Statistics, University of Pittsburgh, Pittsburgh, PA 15213, USA

Jingqin Luo

Department of Surgery, Washington University in St. Louis, St. Louis, MO 63110, USA

Yuichi Motai

Department of Electrical and Computer Engineering, Virginia Commonwealth University, Richmond, VA 23284, USA

Jingfei Ma and John D. Hazle

Department of Imaging Physics, The University of Texas MD Anderson Cancer Center, Houston, TX 77030, USA

H. Michael Gach^{a)}

Departments of Radiation Oncology and Radiology, Washington University, St. Louis, MO 63110, USA

(Received 31 August 2016; revised 14 December 2016; accepted for publication 27 December 2016; published 21 February 2017)

Purpose: Respiratory motion prediction using an artificial neural network (ANN) was integrated with pseudocontinuous arterial spin labeling (pCASL) MRI to allow free-breathing perfusion measurements in the kidney. In this study, we evaluated the performance of the ANN to accurately predict the location of the kidneys during image acquisition.

Methods: A pencil-beam navigator was integrated with a pCASL sequence to measure lung/diaphragm motion during ANN training and the pCASL transit delay. The ANN algorithm ran concurrently in the background to predict organ location during the 0.7-s 15-slice acquisition based on the navigator data. The predictions were supplied to the pulse sequence to prospectively adjust the axial slice acquisition to match the predicted organ location. Additional navigators were acquired immediately after the multislice acquisition to assess the performance and accuracy of the ANN. The technique was tested in eight healthy volunteers.

Results: The root-mean-square error (RMSE) and mean absolute error (MAE) for the eight volunteers were 1.91 ± 0.17 mm and 1.43 ± 0.17 mm, respectively, for the ANN. The RMSE increased with transit delay. The MAE typically increased from the first to last prediction in the image acquisition. The overshoot was $23.58\% \pm 3.05\%$ using the target prediction accuracy of ± 1 mm.

Conclusion: Respiratory motion prediction with prospective motion correction was successfully demonstrated for free-breathing perfusion MRI of the kidney. The method serves as an alternative to multiple breathholds and requires minimal effort from the patient. © 2017 American Association of Physicists in Medicine [https://doi.org/10.1002/mp.12099]

Key words: arterial spin label, artificial neural network, kidney, magnetic resonance imaging, respiratory motion prediction

1. INTRODUCTION

Renal perfusion is an important biomarker for assessing kidney function.¹ Arterial spin labeling (ASL)² is a noninvasive method that uses blood water as an endogenous tracer to measure perfusion in various organs including the kidneys.^{3–9} The principle of measuring the perfusion rate with ASL involves acquiring two images: a labeled image in which the spins (magnetization) of water in the inflowing blood are inverted, and a control image in which the spins are not inverted. The tissue perfusion is proportional to the difference signal from the two images (i.e., control-label).¹⁰

ASL has low perfusion signal-to-noise ratio (SNR), so multiple pairs of the label and control images are typically acquired and the signals are averaged. Therefore, the technique is susceptible to perfusion errors caused by motion. Background suppression, multiple breathholds (including with respiratory feedback or synchronized with image acquisition), respiratory gating to acquire data only when the diaphragm is between a given region, and retrospective sorting of images are used to address the effects of motion.^{8,11}

Breathholds result in a low acquisition efficiency as additional time is required for the patient to recover between breathholds.⁸ The number of acquisitions is limited for each breathhold and the first acquisition may need to be discarded as a steady-state is not usually achieved on the first repetition.⁸ In addition, it is difficult to remain completely motionless and avoid breathhold drift during a moderate to long breathhold (15–20 s), particularly for sick patients.¹² It is also difficult to maintain the same position between different breathholds, even with respiratory feedback.¹³ Alternatively, respiratory gating is not well suited for ASL because of ASL's long repetition time (TR) and the large number of discarded acquisitions expected for a narrow acquisition window.⁸

Real-time organ or landmark position information can be acquired using navigator-echoes.¹⁴ Navigator gating is well suited for imaging sequences with short TRs. However, the technique is poorly suited for ASL or other functional scans (e.g., diffusion weighted imaging) that require a long TR and multiple acquisitions for signal averaging or longitudinal tracking as the anatomical landmark (e.g., lung/diaphragm boundary) typically lies within the acceptance window < 30% of the time.

With prospective motion correction (PMC), navigator-echoes are used to determine the motion of the organ of interest and correct the motion by adjusting the image acquisition in real-time.¹⁵ “Gate and Follow” techniques use a 1D navigator readout and acquire image data if the respiratory landmark lies within the acceptance window after shifting the slice excitation based on the measured displacement. The technique typically works for one slice or slab at a time and may have an acquisition dead time of > 50% assuming short TRs. “Trigger and Follow” techniques use a respiratory training period followed by a 2D navigator readout (typically 100 ms in duration).¹⁶ “Trigger and Follow” is subject to motion during the image acquisition depending on the

number of slices acquired. Prospective motion correction was used in cardiac, liver, and brain studies.^{15,17–20}

Navigators were previously used in ASL with single-slice acquisitions. A 2D navigator was used with flow-sensitive alternating inversion recovery (FAIR) and single-slice true-fast imaging with steady-state precession (True FISP) to permit free-breathing perfusion magnetic resonance imaging (MRI).²¹ Perfusion maps were calculated using control and label images acquired at the same diaphragm position. Cross-pair navigators were used for prospective motion correction with single-slice True FISP FAIR acquisitions in the kidney and for retrospective analysis using True FISP pseudocontinuous ASL (pCASL) in the liver.^{22,23} A navigator-gated, ECG triggered single-slice True FISP FAIR sequence was used to measure cardiac perfusion.²⁴ 3D navigators were used with 3D pCASL acquisitions and prospective motion correction in the brain.²⁵

Much of the innovation in respiratory motion sampling, prediction, and real-time adaptation is being driven by image-guided radiotherapy. Respiratory motion prediction (RMP) was shown to improve the accuracy of image-guided radiotherapy latencies of ≥ 200 ms or sampling rates of ≤ 10 Hz.²⁶

To date, no other MRI studies have implemented RMP in PMC to enable a long latency between the collection of navigator data and the time of image slice acquisition. However, RMP was used in a retrospective analysis of MRIs.^{27,28} The recent availability of integrated MRI-guided radiotherapy has encouraged feasibility studies of integrating RMP in cine-MRI for MRI-guided radiotherapy.^{29,30} For example, a recent simulation showed RMP would decrease MRI-based tracking errors to 0.2–1.2 mm for latencies of 50–300 ms and acquisition times of 25–750 ms.³¹ Therefore, the integration of RMP with 3D and 4D cine-MRI in MRI-guided radiotherapy should be forthcoming.

The artificial neural network (ANN), a flexible tool to model complex nonlinear systems, was used in various MRI applications.^{32,33} Among the various ANN types, the multilayer perceptron is one of the most widely used.³⁴ In this study, we present the first prospective application of RMP in MRI. RMP using pencil-beam navigators³⁵ and a multilayer perceptron ANN was integrated with pCASL³⁶ in a free-breathing acquisition. The purpose of this study was to develop a free-breathing technique that is both efficient in scanning time and accurate in reducing respiration-induced errors. The ANN algorithm was used to predict the kidney position during multislice acquisition for real-time adjustment of the pulse sequence.

2. MATERIAL AND METHODS

The pCASL-RMP technique including the pencil-beam navigator was primarily developed and tested at the University of Pittsburgh MR Research Center. The renal perfusion data were acquired at the Washington University in St. Louis Center for Clinical Imaging Research. All studies were performed on healthy volunteers after informed consent was

obtained in accordance with an Institutional Review Board-approved protocol for the applicable institution. Eight healthy volunteers were scanned on a 3 T mMR (PET/MRI) scanner (Siemens Medical System, Erlangen, Germany).

Volunteers were scanned supine using spine and flexible body phased array coils. A peripheral pulse sensor was placed on their finger for gating arterial velocimetry used in the pCASL inversion efficiency calculations. Respiration was recorded using an air pressure sensor pad and sampled at 50 Hz. The respiratory waveforms were analyzed to compare breathing patterns during ANN training and post-training (i.e., during pCASL image acquisition) by: (a) acquiring the frequency distributions of the respective training and post-training waveforms using a fast Fourier transform and (b) calculating the Pearson's correlation coefficients between the training and post-training frequency distributions.

2.A. Pulse sequence schema

Renal perfusion was measured using a 2D multislice pCASL sequence. A schema of the sequence flow is shown in Fig. 1 and discussed below. The pulse sequences and RMP were implemented using Siemens' integrated development environment for applications (IDEA) and image calculation environment (ICE) compilers (VB20P).

The goal for the RMP was to eliminate the need for respiratory motion measurements between each slice acquisition. In ASL, it is desirable to acquire images as quickly as possible after the transit delay as the ASL tracer is decaying with the T_1 of the tracer (e.g., blood). The use of "Trigger and Follow" typically requires the insertion of a navigator before each slice acquisition, thereby reducing the image acquisition duty efficiency by 30–50% for echo planar imaging (EPI). The successful RMP would maintain a high imaging efficiency while still allowing the slice to follow the motion of the organ.

2.B. Pencil-beam navigator

We substituted a 1D pencil-beam navigator using a 2D excitation with spiral trajectory (flip angle = 10° , TE/TR = 4/100 ms, excitation radius = 10 mm, readout pixel size = 0.5 mm, readout coverage = 256 mm) for the standard Siemens cross-pair (90° – 180°) navigator to permit consistent navigator profiles.³⁵ The duration of the navigator excitation and readout was < 15 ms. The aim of the navigator was to acquire a 1D profile in the cranial–caudal direction to determine the diaphragm position. The navigator was

executed during 19-s scouts to identify a location in the top right dome of the liver that yielded a satisfactory respiratory trace.

Navigator-echoes were acquired for 60 s to train the ANN. The navigator-echoes were acquired consecutively and reconstructed into 1D profiles in real-time using ICE. The diaphragm displacement was calculated by comparison with the first (reference) navigator profile. Based on lessons learned, a 20-s delay was placed between the end of the navigator-echo acquisitions and the start of the pCASL acquisitions to ensure the ICE program had sufficient time to calculate the ANN weights particularly in the case of complex breathing or noisy navigator data.

During the pCASL transit delay, navigator-echoes were acquired to measure the diaphragm position as input to the ANN for prediction of respiratory motion in the pCASL multislice acquisition. During the TR fill time (i.e., immediately after the image acquisition and before the start of the next repetition), navigators were acquired to assess ANN prediction performance by comparing the predictions with actual displacements.

2.C. pCASL EPI Sequence

An unbalanced pCASL sequence was used for this study with: TE/TR: 18/7500 ms, label time/transit delay: 1.6/1.5 s, label flip angle: 28.7° , label gradient flattop: 11 mT/m, mean labeling gradient: 0.8 mT/m, slice thickness: 5 mm, 15 slices, FOV: 260–330 mm, acquisition matrix: 64×64 , receiver bandwidth: 3000 Hz/pixel, 7/8 partial k-space. Normally, the TR was set to 5 s but we added an additional 2.5 s after the image acquisition to acquire supplementary navigators and evaluate the performance of the RMP in the volunteers for this study. Axial 2D multislice EPI images were acquired at 50 ms/slice.³⁶

The labeling plane was placed inferior to the lung/diaphragm boundary (superior to the kidneys) to minimize interference of the labeling/control irradiation and the navigator magnetization and the effects of field inhomogeneity on labeling efficiency associated with the lung/tissue susceptibility.³⁷

With RMP, there are two considerations for choosing the transit delay: (a) The transit delay allows the labeled spins to arrive at the kidney tissue but not longer as the label is decaying with a relaxation time of T_1 ; and (b) Enough navigator measurements are acquired to enable adequate prediction precision. Each volunteer was scanned twice with the pCASL-RMP sequence and once with free-breathing pCASL without

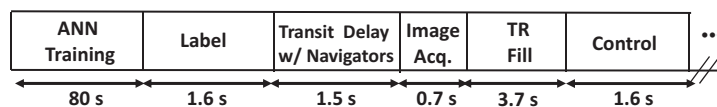


FIG. 1. Pulse sequence schema. The 80-second artificial neural network (ANN) training included 60 s for navigator-echo acquisitions and a 20-s pause for ANN computation and optimization. The training was performed at the beginning of the pseudocontinuous arterial spin labeling–respiratory motion prediction (pCASL-RMP) sequence. The pCASL irradiations were 1.6 s followed by a 1.5-s transit delay that included the navigators for measuring respiratory motion. We acquired 15 imaging slices in 0.7 s. We added an optional 3.7 s TR fill period that included 37 navigators for assessing RMP performance.

navigators and RMP (same parameters except the TR was 5 s).

2.D. Data processing of navigators

The navigator profile was first interpolated between two neighbor pixels to achieve a resolution of 0.25 mm in the readout direction. The navigators were normalized to address amplitude variations. A reference navigator was chosen at the beginning of the training phase and placed at the diaphragm and liver boundary. The reference navigator profile ranged between ± 30 mm with the center of the profile located at 0 mm. The displacement \hat{d} was determined by minimizing the sum of squared errors between the reference and input navigators. A tracking factor of 0.7 was used to convert the diaphragm displacement to a kidney displacement based on the literature and our preliminary volunteer tests.³⁸

2.E. Artificial neural network

A three-layer ANN was implemented with $n_1 = 15$, $n_2 = 10$, $n_3 = 7$ number of nodes on each layer, respectively. A time-delayed vector of diaphragm displacement $[\hat{d}(t - \tau), \hat{d}(t - 2\tau), \dots]$ was fed to the nodes in the input layer where τ is the navigator TR. We sampled the displacement every 100 ms (τ) to properly characterize the dynamics of the trajectory, avoiding unnecessary random fluctuations from sampling too frequently.

The ANN was compiled using ICE and executed on the MR image reconstruction (MRIR) computer. Navigator displacements were sent continuously to the measurement and physiologic control unit (MPCU) and logged. After the final navigator in the transit delay, the predictions for the 2D slice excitations were transmitted to the MPCU where they were converted into slice excitation frequency offsets by the pulse sequence based on the slice acquisition timing and uploaded to the RF digital signal processor in real-time. The final navigator period was fixed at 100 ms to ensure adequate time for the MRIR-MPCU communications and implementation of the slice frequency offsets.

The performance of the ANN predictions was assessed in two ways. First, the prediction performance was evaluated in real-time by applying the ANN to the TR fill navigator data, starting from the first navigator in the TR fill, and using a moving window with the same length as the transit delay (nominally 15 navigators). The ANN prediction errors were calculated by using the successive navigator-echo measurements occurring after the window's input displacements. The calculation was re-performed by incrementally moving the window forward in time until the end of the TR fill time was encountered. In addition, we varied the length of the moving window to assess the effects of the transit delay (i.e., number of input nodes) on the prediction accuracy during off-line simulations.

Second, we analyzed the correspondence between the last navigator acquired in the transit delay and the first prediction,

and the last prediction and the second navigator acquired during the TR fill. The first navigator in the TR fill (postimaging) was not used because we observed that the liver magnetization was affected by image acquisition (images were acquired from foot to head), particularly when the distance between the liver dome and the superior portion of the kidney was small.

For all comparisons, absolute prediction errors and root-mean-square errors (RMSE) were calculated between the ANN prediction and the navigator-echo displacements. The overshoot was calculated as the percentage of predictions that exceeded the targeted precision. We chose a target precision magnitude of 1 mm for three reasons: (a) the spatial resolution of the original 1D cross-pair navigator was 1 mm; (b) preliminary studies indicated that 1 mm predictor precision was challenging but achievable; and (c) through-plane subtraction errors were assumed to decrease with a decreasing ratio of tracking precision to slice thickness. The 1-mm target was intended to ensure subtraction errors were dominated by in-plane motion often observed as hypoperfusion or hyperperfusion at the periphery of the kidneys. By comparison, breathholds tended to be subject to diaphragm drift of ~ 2 mm in the cranial-caudal direction, whereas free-breathing could result in diaphragm excursions of 2–3 cm.¹²

2.F. pCASL inversion efficiency

The mean inversion efficiency of the pCASL sequence was calculated for typically 5–6 cardiac phases at the labeling plane. The inversion efficiency for each cardiac phase $\langle \alpha_i \rangle$ was calculated based on a Zhernovoi model³⁹ for adiabatic fast passage, and modified for pCASL:

$$\langle \alpha_i \rangle = 1 - \exp \left[\frac{-\pi \gamma \langle B_l \rangle^2}{2 \langle \bar{G}_l \rangle \bullet \langle \bar{v}_i \rangle} \right] \quad (1)$$

where γ is the gyromagnetic ratio for proton, v_i is the arterial blood velocity measured at the labeling plane for cardiac phase i , and $\langle B_l \rangle$ and $\langle G_l \rangle$ are the mean pCASL labeling RF and gradient amplitudes, respectively. Alternatively, one can calculate the inversion efficiency by solving the Bloch equations but we found the results were equivalent. The mean velocity of blood in the descending aorta ($\langle v_i \rangle$) was measured for each cardiac phase at the pCASL labeling plane using a single-slice phase contrast cine gradient echo sequence: TE/TR: 10/150 ms, FA: 15 degrees, slice thickness: 5 mm, FOV: 300×300 mm², Matrix: 256×256 , $v_{enc} = 120$ cm/s, rBW: 260 Hz/pixel.

A region of interest was drawn within the lumen of the descending aorta for each cardiac phase and the mean image phase was calculated and converted into a mean velocity $\langle v_i \rangle$. The volume flow rate (Q_i) for each cardiac phase was calculated as the product of $\langle v_i \rangle$ and the corresponding lumen area A_i . The mean inversion efficiency for the cardiac cycle was calculated as:

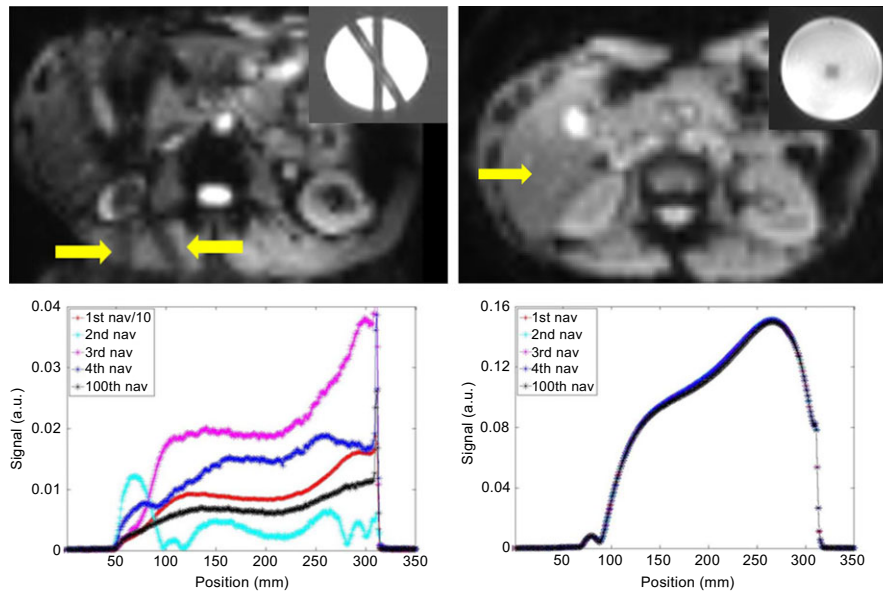


FIG. 2. Comparison of cross-pair (left column) and pencil-beam (right column) navigators (repetition time: 100 ms) in axial slices shows that the pencil-beam navigator resulted in a reduced saturation profile (top row) and uniform navigator profiles (bottom row). The first profile for the cross-pair navigator was divided by 10 to enable comparison with the successive navigator profiles. The saturation (insets) and navigator profiles were measured in an agar phantom ($T_1 = 1.7$ s at 3 T). [Colour figure can be viewed at wileyonlinelibrary.com]

$$\langle \alpha \rangle = \frac{\sum_i \langle \alpha_i \rangle \cdot Q_i}{\sum_i Q_i} \quad (2)$$

2.G. Perfusion quantification

The quantitative renal blood flow was calculated using:²

$$f = \frac{\lambda}{2 \langle \alpha \rangle T_{1a} \left[\exp\left(\frac{\tau - t_{acq}}{T_{1a}}\right) - \exp\left(\frac{-t_{acq}}{T_{1a}}\right) \right]} \frac{\Delta M}{M_c} \quad (3)$$

where f is the perfusion rate in ml/100 g-min, λ is the blood-tissue water partition coefficient which was assumed to be a constant value of 0.8 ml/g (Ref. 3), $\langle \alpha \rangle$ is the inversion efficiency as discussed above, ΔM is the mean difference signal (control-label), t_{acq} is the time of image acquisition relative to the start of the label pulse train, τ is the label pulse train duration, M_c is the mean unlabeled MRI signal, and T_{1a} is the longitudinal relaxation time of the arterial blood, (1.5 s at 3 T⁴⁰). We assumed the transit delay was longer than the tracer arrival time yet ignored relaxation time changes associated with tracer exchange with the tissue compartment.

We manually segmented the kidneys based on the first repetition of each acquisition. Pixels with negative perfusion values or values > 750 ml/100 g-min were excluded. We set an upper perfusion cutoff and lower perfusion threshold for renal medulla and cortex, respectively, at 150 ml/100 g-min as the low in-plane resolution and partial volume prevented us from clearly delineating the cortex from the medulla in the images.^{5,7,41,42}

3. RESULTS

3.A. Respiratory motion estimation

Figure 2 depicts the advantages of the pencil-beam navigator for the pCASL-RMP pulse sequence. First, the pencil-beam navigator has a smaller saturation profile than the cross-pair navigator, and the former minimizes saturation of the perfusion volume of interest. Second, the profiles for the pencil-beam navigator are consistent and uniform between successive measurements.

3.B. ANN prediction

Figure 3 shows the mean absolute error (MAE) and distribution for the eight volunteers using the ANN predictor and the nominal 1.5-s transit delay. The MAE was 1.43 ± 0.14 mm. The RMSE for the eight volunteers was 1.91 ± 0.17 mm for the ANN. The overshoot was $23.58 \pm 3.05\%$ using the target prediction accuracy of ± 1 mm.

Figure 4 provides an example of the navigator displacements and ANN predictions for one of the volunteers. Figure 5 shows the absolute difference between the last transit delay navigator and the first prediction (LNFP), and the last prediction and second TR fill navigator (LP2N). Using a ± 1 -mm criterion, the acceptance rate averaged over the eight subjects was $60.78 \pm 8.77\%$ using the first prediction (LNFP) and $32.5 \pm 7.97\%$ based on the last prediction (LP2N). The mean absolute differences for the eight volunteers were 1.47 ± 0.43 mm (LNFP) and 2.32 ± 0.37 mm (LP2N). The RMSEs for the eight volunteers were 1.96 ± 0.55 mm (LNFP) and 2.97 ± 0.49 mm (LP2N).

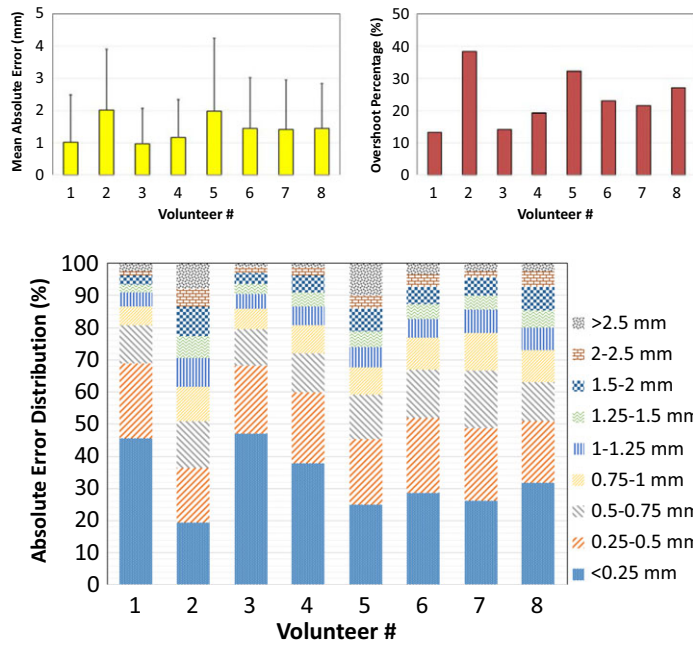


FIG. 3. Top left: Mean absolute errors and their standard deviations (error bars) for the eight volunteers using the nominal 1.5-s transit delay. Top right: Overshoot percentage for each volunteer. Bottom: The corresponding absolute error distribution (%) by volunteer and error interval. A total of 71,360 predictions were included in the analysis. [Colour figure can be viewed at wileyonlinelibrary.com]

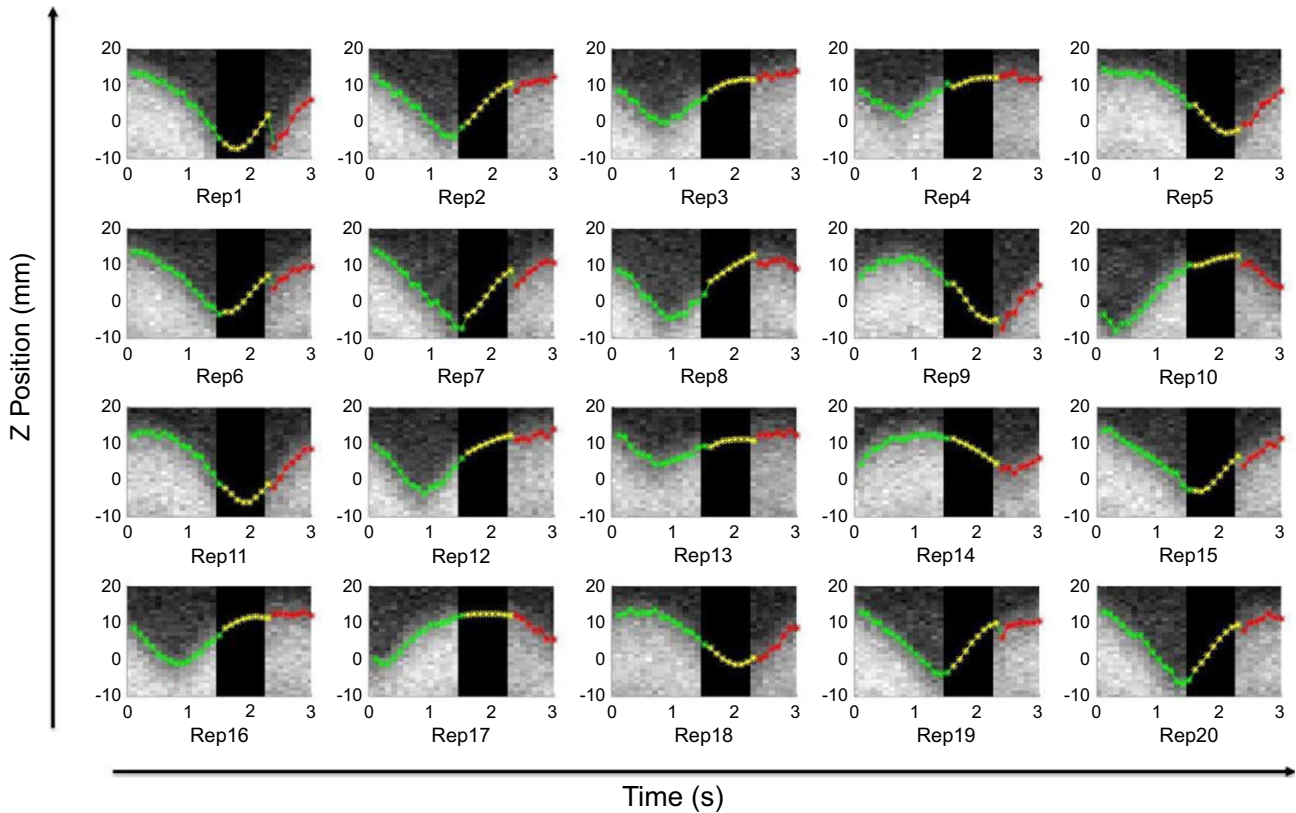


FIG. 4. Example of navigator displacements and artificial neural network (ANN) predictions covering the first 10 label/control pairs (20 repetitions) during a pseudocontinuous arterial spin labeling acquisition in Subject #4. The gray scale profile was reconstructed from the navigator data and shows the diaphragm position during each repetition. The dotted plot shows the measured displacements before (0 to 1.4 s) and after (2.3 to 3 s) image acquisition, as well as the ANN predictions during (1.5 to 2.2 s) image acquisition. Only the first 7 of 37 post-imaging navigators are shown in each for easy viewing. [Colour figure can be viewed at wileyonlinelibrary.com]

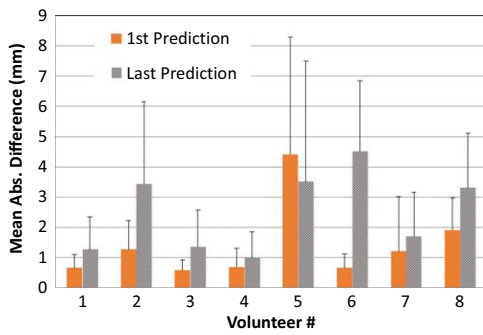


FIG. 5. Absolute difference between the last navigator in the 1.5-s transit delay and the first prediction for the image acquisition (solid bars) and absolute difference between the last prediction in the image acquisition and the second navigator acquired post-imaging (hatched bars). The differences were averaged over the 40 repetitions acquired for each volunteer. The error bars represent the standard deviations. [Colour figure can be viewed at wileyonlinelibrary.com]

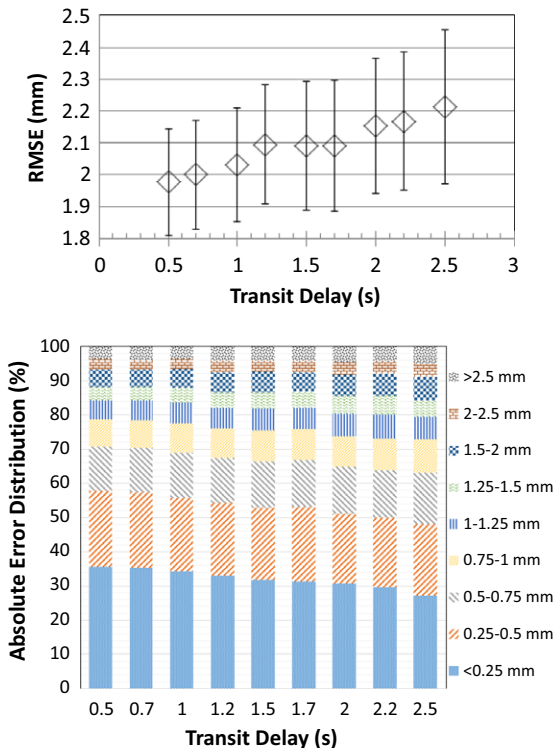


FIG. 6. Results of prediction error simulation using the postimaging navigators. Top: Root-mean-square error (RMSE) as a function of transit delay averaged over the eight volunteers. Bottom: Absolute error distribution (%) by transit delay and error interval averaged over the eight volunteers. [Colour figure can be viewed at wileyonlinelibrary.com]

Figure 6 shows the effects of varying the transit delay (i.e., the number of ANN inputs before imaging) on the prediction RMSE and includes the absolute error distribution. According to the analysis, the prediction accuracy generally degrades with increasing transit delay. Please note that the RMSE for the 1.5-s transit delay in Fig. 6 is slightly higher (2.09 ± 0.20 mm) than that of Fig. 3. The reason is that Fig. 3 data came from the real-time ICE calculations generated during the MRI and recorded to a log file, whereas the

Fig. 6 results were calculated during the off-line simulations. The discrepancy is related to the differences in initialization of the ANN (i.e., the random seed) and that the simulation included all of the postimaging navigators (the first log file for Volunteer 1 was incomplete).

3.C. Renal perfusion measurement

The demographics for our volunteers are shown in Table I. We did not observe any significant covariates for renal perfusion given our small sample size. Table I includes the Pearson’s correlation coefficients resulting from the analysis of the respiratory sensor data between the ANN training and pCASL post-training periods. The renal perfusion values for combined, cortex, and medulla are shown in Table II. An example of the perfusion maps for one of the volunteers is shown in Fig. 7. The mean inversion efficiency for the eight volunteers was 0.9435 ± 0.01 .

4. DISCUSSION

4.A. Navigator profile and processing

The substitution of a pencil-beam navigator for the cross-pair navigator was critical to the performance of the RMP. Consistent profiles facilitated the accurate calculation of displacements. The pencil-beam navigator successfully measured diaphragm motion along the cranial–caudal direction at the high sampling rate required for the ANN. A pencil-beam navigator was previously used for navigator-gated pCASL of the kidney.⁴³

We tested several different flip angles for the navigator. A 10° flip angle was significantly lower than the Ernst angle ($\sim 28^\circ$ for liver) for a 100 ms TR. However, the primary concern was to generate consistent navigator profiles to ensure the displacement calculation was not affected by a transient state. In addition, the lower flip angle minimizes the saturation of the imaging volume of interest. Despite the low navigator flip angle, the navigator-echo SNR was high at 3 T and we were able to get quality traces.

The technique was sensitive to the positioning of the navigator. It often took several attempts to position the navigator for a clear trace as individuals have unique breathing patterns. Even if the trace was clear, it may not have represented the full range of motion. We also observed that the navigator trace sometimes changed during the exam (e.g., after deep breathholds) and the position of the navigator had to be updated.

The fixed tracking factor (i.e., 0.7) may have increased the ANN prediction error as the relationship between diaphragm and kidney displacement varies between individuals. In principle, the tracking factor should be measured for each individual although this may increase examination time and the burden on the technologist.

It is possible to use respiratory sensor (e.g., bellows or pressure pad) data as an alternative or complement to the

TABLE I. Volunteer demographics and breathing correlations.

Subject #	Age	Gender	Body mass index	Race	Mean Pearson's correlation coefficient between ANN training and post-training respiratory frequency distributions*
1	22	Female	24.36	Caucasian	0.9830 ± 0.0064
2	21	Male	31.87	Caucasian	0.9787 ± 0.0046
3	23	Female	21.03	Asian	0.9829 ± 0.0051
4	31	Male	25.10	Asian	0.9661 ± 0.0090
5	20	Female	16.99	Caucasian	0.9654 ± 0.0184
6	21	Female	21.45	Asian	0.9447 ± 0.0261
7	27	Male	33.24	African-American	0.9793 ± 0.0060
8	34	Female	21.73	Asian	0.9911 ± 0.0036
Mean	24.88 ± 1.85	38% Male	24.47 ± 1.97	38% Caucasian	0.9739 ± 0.0048

*All *P*-values are $\ll 0.0001$.

navigator-echo data.⁴⁴ However, respiratory sensor signals are typically processed with autoring and the signals are not directly proportional to respiratory displacements. Respiratory sensor data are also prone to drift (e.g., movement of the sensor during the exam) and contamination from cardiac motion. The sensor data are best used to distinguish respiratory phase.

4.B. ANN prediction algorithm

The accuracy of the ANN prediction algorithm depended on several factors. First, the training phase of the ANN algorithm was crucial for the prediction performance as the predictions were based on the training respiratory patterns. We reserved 80 s for ANN training and processing, although a shorter time may be used for subjects with well-behaved breathing. Second, decreasing the number of input nodes and/or decreasing the number of output nodes of the algorithm increased the accuracy of the prediction performance. The number of nodes in the hidden layer was not so critical in the prediction performance, as long as its value was between the number of input nodes and output nodes, and bridged the connections between them.

Finally, the prediction error typically increased with latency. Based on Fig. 5, the difference between navigator displacement and prediction typically increased from the first to last prediction. The latency between the last transit delay navigator and the first prediction was 100 ms, whereas the virtual time difference between the last prediction and the second TR fill navigator was ~150 ms. In practice, all of the predictions were calculated before the end of the transit delay so the latency between the last prediction and the second TR fill navigator was ~900 ms. Therefore, it is not surprising that the absolute error is higher for the last prediction.

A transit delay of 1.5 s was a compromise between the performance of the RMP and the magnitude of ASL difference signal. The ASL tracer was decaying with T_1 during the transit delay. It is desirable to maintain the transit delay to be just larger than the tracer's transit time from the labeling plane to the parenchyma. The transit time to the kidney was

estimated to be 0.4–1.5 s depending on the cardiac cycle.^{45,46} Our results indicate that the prediction error tended to increase with increasing transit delay based on multiple volunteers.

The ANN was not designed to adapt to breathing changes that occurred between training and image acquisition. This requires an RMP method that updates the prediction network while the sequence is running, e.g., using the navigator displacements acquired after training. Once successfully trained, the navigator processing time for the current version of the ANN was less than 10 ms. Nevertheless, the analysis of the respiratory frequency distributions measured from the respiratory sensor indicated high correlations between respiratory behavior during and after ANN training (Table I).

We tested two navigator sampling rates (10 and 20 Hz) and did not observe a significant difference in prediction accuracy. A 100-ms period was desirable as we needed to ensure adequate time for the predictions to be converted into frequency offsets and loaded in the digital signal processors. In addition, higher sampling rates increase the computational burden of the ANN training period.

The choice of prediction algorithm is critical. We evaluated a variety of linear and stochastic algorithms using MRI and image-guided radiotherapy data.^{47–52} The piecewise linear sample path model and a weighted Fourier linear combiner both showed promise for the pCASL application.^{53,54} We also tested the constant velocity and acceleration Kalman filter⁵⁵ using MRI data but found it could not track respiratory nonlinearities. We selected the ANN for its performance, flexibility, low computational requirements, and ease of implementation in the IDEA/ICE environment. Nevertheless, prediction algorithms with improved accuracy, particularly for irregular breathing, are needed.

4.C. Renal perfusion

The resulting perfusion values are consistent with past studies.^{7,42} As our main objective was evaluating the performance of the ANN predictor, we did not apply advanced perfusion quantification methods for this study. Therefore, the

TABLE II. Renal perfusion values (ml/100 g-min) for healthy volunteers.

Subject #	Combined						Cortex			Medulla		
	Run 1	Run 2	No RMP	Run 1	Run 2	No RMP	Run 1	Run 2	No RMP	Run 1	Run 2	No RMP
	1	206.19	240.97	222.38	317.23	313.74	291.16	73.68	79.95	80.06	73.68	79.95
2*	188.87	181.19	116.18	316.93	286.95	264.70	66.09	75.64	59.70	66.09	75.64	59.70
3	111.99	117.73	184.04	247.68	244.58	304.43	63.10	63.35	70.08	63.10	63.35	70.08
4*	166.36	185.29	205.88	251.49	321.08	325.43	81.33	72.85	72.02	81.33	72.85	72.02
5	219.94	190.10	217.83	315.76	315.73	332.58	73.77	70.79	75.02	73.77	70.79	75.02
6*	136.49	249.84	130.17	236.87	319.57	279.00	75.78	77.22	62.93	75.78	77.22	62.93
7*	162.03	178.3	132.46	290.81	327.86	269.36	68.94	70.03	67.08	68.94	70.03	67.08
8*	199.76	230.45	144.85	312.92	318.35	262.80	72.93	77.55	73.47	72.93	77.55	73.47
Mean	173.95 ± 13.01	196.73 ± 15.18	169.22 ± 15.26	286.21 ± 12.42	305.98 ± 9.76	291.18 ± 9.63	71.95 ± 2.03	73.42 ± 1.89	70.05 ± 2.34	71.95 ± 2.03	73.42 ± 1.89	70.05 ± 2.34

*Operational changes made between 1st and 2nd run. RMP, respiratory motion prediction.

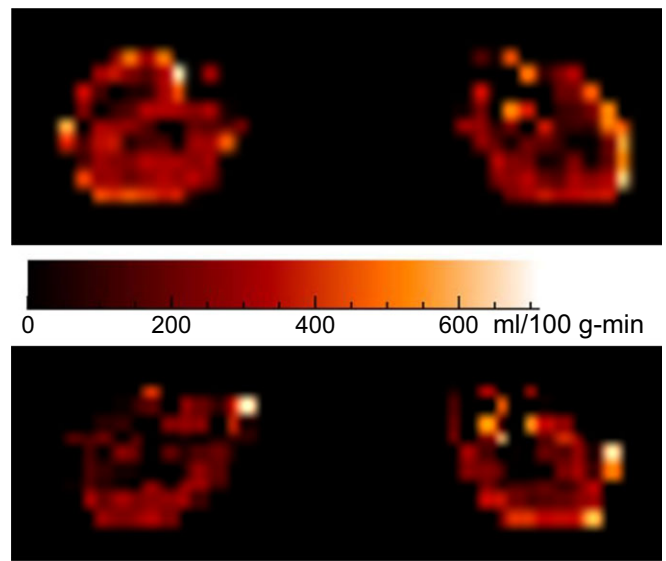


FIG. 7. Renal perfusion maps from Subject #1 using pseudocontinuous arterial spin labeling with (above color scale) and without (below color scale) respiratory motion prediction. [Colour figure can be viewed at wileyonlinelibrary.com]

perfusion maps can be further improved using sorting or discarding of images, B_1 corrections to address variations in acquisition position, and improved kidney segmentation, alignment, and coregistration.^{8,56}

We did not observe a significant difference in perfusion between the repetitions or between RMP and free-breathing pCASL, similar to a previous study.¹¹ A correlation analysis indicated that perfusion variance rose as the mean absolute prediction error increased but the results were not statistically significant ($P \geq 0.07$). Nevertheless, the intersection of the imaging slice and kidney is generally more consistent for pCASL with breathhold and RMP versus free-breathing (Fig. 8). Therefore, free-breathing pCASL may be adequate for assessing global renal perfusion, whereas pCASL with breathhold or RMP may be better suited for assessing localized perfusion.

The technique was applied to axial slice acquisition for which the primary component of respiratory motion is through-plane, thus representing the greatest challenge for the RMP-PMC technique. Other renal ASL studies used coronal or sagittal acquisitions which are less sensitive to respiratory motion as the primary components of the motion are in-plane and can be corrected in postprocessing using image co-registration. However, coronal or sagittal acquisitions may perturb the magnetization of the endogenous tracer during inversion or transit unless the prescription is adjusted to avoid the supplying arteries and the heart.⁵ Axial acquisitions may permit smaller fields-of-view (higher image resolution) and reduce the risk that imaging will affect the magnetization used by a navigator (e.g., for retrospective image sorting).

For this study, we acquired low-resolution EPI images (matrix: 64×64 resulting in ~ 4.7 mm in-plane resolution) to cover the volume including the kidney. We successfully

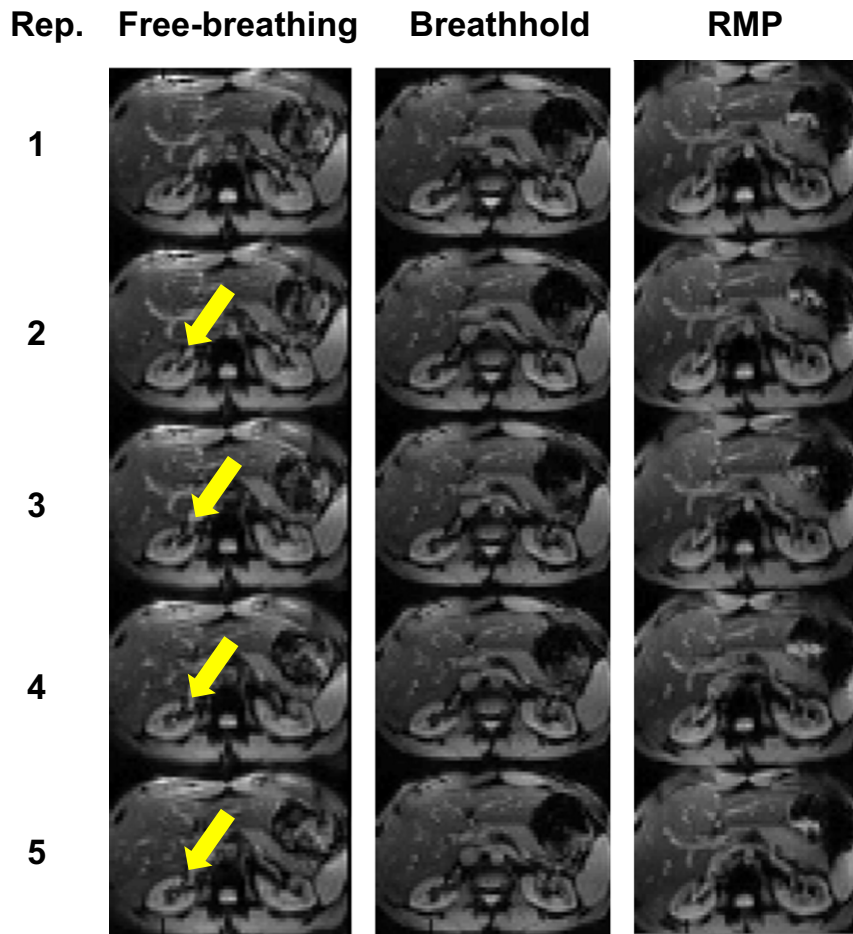


FIG. 8. Comparison of renal positioning variations during pseudocontinuous arterial spin labeling with free-breathing (left), breathhold (middle), and respiratory motion prediction (right) for five repetitions acquired from one of the authors. Shown is slice 6 of 12 (repetition time: 5 s). Variations are noticeable (arrows) in the free-breathing acquisitions. Respiratory feedback was used to minimize diaphragm drift during the breathhold. However, we did not acquire additional sequences to permit quantification of perfusion for this experiment. [Colour figure can be viewed at wileyonlinelibrary.com]

tested the RMP-PMC technique using 128×128 (2.4 mm resolution) EPI acquisitions. However, the longer acquisitions require a corresponding reduction in the total number of slices acquired as an increase in the latency will result in decreased prediction accuracy. In other renal ASL perfusion studies, anywhere from 1 to 34 slices are acquired using single-shot and multi-shot techniques typically with in-plane resolutions of >2.5 mm.^{8,43,57} In addition, the longer EPI acquisition may reduce the perfusion SNR and increase artifacts that are common in low-resolution EPI images in the abdomen. Improved fat saturation or rejection, B_0 shimming, and pulse sequence optimization strategies may reduce the artifacts.

RMP can be integrated with background suppression.⁵⁸ The navigators can be run in between the background suppression and superior saturation pulses during the transit delay.¹¹ We observed that in some of the volunteers, the distance between the top of the superior kidney and the right dome of the liver can be small (<5 cm). This presents a challenge as it is important that the labeling plane and background suppression leave several centimeters of the superior portion of the liver undisturbed

to maintain the consistency and integrity of the navigator trace.

As far as we know, this is the first application of RMP for PMC of MRI. It is an extension of “Trigger and Follow”. The integration of RMP in ASL represents a challenging application as latencies can range up to 1 s. However, the technique can be adapted to other sequences with long latencies, e.g., diffusion tensor imaging, 4D MRI, and $T_{1\rho}$.^{59,60}

5. CONCLUSIONS

In conclusion, multislice pCASL with RMP allows free-breathing measurements of renal perfusion without substantially increasing examination time or requiring patient effort for breathholding. Nevertheless, further work is required to improve the prediction accuracy of the RMP and the quality of the perfusion maps.

ACKNOWLEDGMENTS

This research was conducted primarily with the support of National Institutes of Health National Cancer Institute grant

R01 CA159471. Our research also received support from the Nevada Cancer Institute, the University of Pittsburgh, Washington University in St. Louis, The University of Texas MD Anderson Cancer Center, and UCLA. We are indebted to Cornell University's Yi Wang, Than Nguyen, and Pascal Spincemaille for providing technical expertise during the formative period of this project. We also appreciate the technical assistance of Siemens Healthcare, especially Agus Priatna, Tiejun Zhao, Vibhas Deshpande, and Mark Brown. We thank Tamara Locke from The University of Texas MD Anderson Cancer Center for editing our manuscript.

CONFLICTS OF INTEREST

The authors have no relevant conflicts of interest to disclose.

^{a)}Author to whom correspondence should be addressed. Electronic mail: gachhm@wustl.edu.

REFERENCES

- Huang AJ, Lee VS, Rusinek H. Functional renal MR imaging. *Magn Reson Imaging Clin N Am*. 2004;12:469–486, vi.
- Detre JA, Leigh JS, Williams DS, Koretsky AP. Perfusion imaging. *Magn Reson Med*. 1992;23:37–45.
- Roberts DA, Detre JA, Bolinger L, et al. Renal perfusion in humans: MR imaging with spin tagging of arterial water. *Radiology*. 1995;196:281–286.
- Karger N, Biederer J, Lusse S, et al. Quantitation of renal perfusion using arterial spin labeling with FAIR-UFLARE. *Magn Reson Imaging*. 2000;18:641–647.
- Martirosian P, Klose U, Mader I, Schick F. FAIR true-FISP perfusion imaging of the kidneys. *Magn Reson Med*. 2004;51:353–361.
- De Bazelaire C, Rofsky NM, Duhamel G, Michaelson MD, George D, Alsop DC. Arterial spin labeling blood flow magnetic resonance imaging for the characterization of metastatic renal cell carcinoma. *Acad Radiol*. 2005;12:347–357.
- Fenchel M, Martirosian P, Langanke J, et al. Perfusion MR imaging with FAIR true FISP spin labeling in patients with and without renal artery stenosis: initial experience. *Radiology*. 2006;238:1013–1021.
- Robson PM, Madhuranthakam AJ, Dai W, Pedrosa I, Rofsky NM, Alsop DC. Strategies for reducing respiratory motion artifacts in renal perfusion imaging with arterial spin labeling. *Magn Reson Med*. 2009;61:1374–1387.
- Cutajar M, Thomas DL, Banks T, Clark CA, Golay X, Gordon I. Repeatability of renal arterial spin labelling MRI in healthy subjects. *MAGMA*. 2012;25:145–153.
- Buxton RB, Frank LR, Wong EC, Siewert B, Warach S, Edelman RR. A general kinetic model for quantitative perfusion imaging with arterial spin labeling. *Magn Reson Med*. 1998;40:383–396.
- Robson PM, Madhuranthakam AJ, Smith MP, et al. Volumetric arterial spin-labeled perfusion imaging of the kidneys with a three-dimensional fast spin echo acquisition. *Acad Radiol*. 2016;23:144–154.
- Holland AE, Goldfarb JW, Edelman RR. Diaphragmatic and cardiac motion during suspended breathing: preliminary experience and implications for breath-hold MR imaging. *Radiology*. 1998;209:483–489.
- Wang Y, Grimm RC, Rossman PJ, Debbins JP, Riederer SJ, Ehman RL. 3D coronary MR angiography in multiple breath-holds using a respiratory feedback monitor. *Magn Reson Med*. 1995;34:11–16.
- Taylor AM, Jhooti P, Wiesmann F, Keegan J, Firmin DN, Pennell DJ. MR navigator-echo monitoring of temporal changes in diaphragm position: implications for MR coronary angiography. *J Magn Reson Imaging*. 1997;7:629–636.
- Lee CC, Jack CR Jr, Grimm RC, et al. Real-time adaptive motion correction in functional MRI. *Magn Reson Med*. 1996;36:436–444.
- Klessen C, Asbach P, Kroencke TJ, et al. Magnetic resonance imaging of the upper abdomen using a free-breathing T2-weighted turbo spin echo sequence with navigator triggered prospective acquisition correction. *J Magn Reson Imaging*. 2005;21:576–582.
- Zech CJ, Herrmann KA, Huber A, et al. High-resolution MR-imaging of the liver with T2-weighted sequences using integrated parallel imaging: comparison of prospective motion correction and respiratory triggering. *J Magn Reson Imaging*. 2004;20:443–450.
- McConnell MV, Khasgiwala VC, Savord BJ, et al. Prospective adaptive navigator correction for breath-hold MR coronary angiography. *Magn Reson Med*. 1997;37:148–152.
- Thesen S, Heid O, Mueller E, Schad LR. Prospective acquisition correction for head motion with image-based tracking for real-time fMRI. *Magn Reson Med*. 2000;44:457–465.
- Pedersen H, Kelle S, Ringgaard S, et al. Quantification of myocardial perfusion using free-breathing MRI and prospective slice tracking. *Magn Reson Med*. 2009;61:734–738.
- Tan H, Koktzoglou I, Prasad PV. Renal perfusion imaging with two-dimensional navigator gated arterial spin labeling. *Magn Reson Med*. 2014;71:570–579.
- Pan X, Qian T, Fernandez-Seara MA, et al. Quantification of liver perfusion using multidelay pseudocontinuous arterial spin labeling. *J Magn Reson Imaging*. 2016;43:1046–1054.
- Song R, Loeffler RB, Hillenbrand CM. Improved renal perfusion measurement with a dual navigator-gated Q2TIPS fair technique. *Magn Reson Med*. 2010;64:1352–1359.
- Wang DJ, Bi X, Avants BB, Meng T, Zuehlsdorff S, Detre JA. Estimation of perfusion and arterial transit time in myocardium using free-breathing myocardial arterial spin labeling with navigator-echo. *Magn Reson Med*. 2010;64:1289–1295.
- Zun Z, Shankaranarayanan A, Zaharchuk G. Pseudocontinuous arterial spin labeling with prospective motion correction (PCASL-PROMO). *Magn Reson Med*. 2014;72:1049–1056.
- Sharp GC, Jiang SB, Shimizu S, Shirato H. Prediction of respiratory tumour motion for real-time image-guided radiotherapy. *Phys Med Biol*. 2004;49:425–440.
- Positano V, Bernardeschi I, Zampa V, Marinelli M, Landini L, Santarelli MF. Automatic 2D registration of renal perfusion image sequences by mutual information and adaptive prediction. *MAGMA*. 2013;26:325–335.
- Tanner C, Samei G, Szekely G. Improved reconstruction of 4D-MR images by motion predictions. *Med Image Comput Assist Interv*. 2014;17:146–153.
- Mutic S, Dempsey JF. The ViewRay system: magnetic resonance-guided and controlled radiotherapy. *Semin Radiat Oncol*. 2014;24:196–199.
- Lagendijk JJ, Raaymakers BW, van Vulpen M. The magnetic resonance imaging-linac system. *Semin Radiat Oncol*. 2014;24:207–209.
- Seregni M, Paganelli C, Lee D, et al. Motion prediction in MRI-guided radiotherapy based on interleaved orthogonal cine-MRI. *Phys Med Biol*. 2016;61:872–887.
- Bagher-Ebadian H, Jain R, Paudyal R, et al. Magnetic resonance estimation of longitudinal relaxation time (T_1) in spoiled gradient echo using an adaptive neural network. In: *2011 International Joint Conference on Neural Networks (IJCNN)*. San Jose: IEEE; 2011: 2557–2562.
- Bagher-Ebadian H, Nagaraja TN, Paudyal R, et al. MRI estimation of contrast agent concentration in tissue using a neural network approach. *Magn Reson Med*. 2007;58:290–297.
- Gardner MW, Dorling SR. Artificial neural networks (the multilayer perceptron) – A review of applications in the atmospheric sciences. *Atmos Environ*. 1998;32:2627–2636.
- Nehrke K, Bornert P, Groen J, Smink J, Bock JC. On the performance and accuracy of 2D navigator pulses. *Magn Reson Imaging*. 1999;17:1173–1181.
- Dai W, Garcia D, de Bazelaire C, Alsop DC. Continuous flow-driven inversion for arterial spin labeling using pulsed radio frequency and gradient fields. *Magn Reson Med*. 2008;60:1488–1497.
- Jahanian H, Noll DC, Hernandez-Garcia L. B_0 field inhomogeneity considerations in pseudo-continuous arterial spin labeling (pCASL): effects

- on tagging efficiency and correction strategy. *NMR Biomed.* 2011;24:1202–1209.
38. Song R, Tipirneni A, Johnson P, Loeffler RB, Hillenbrand CM. Evaluation of respiratory liver and kidney movements for MRI navigator gating. *J Magn Reson Imaging.* 2011;33:143–148.
 39. Zhernovoi AI. Fast adiabatic passage in nuclear magnetic resonance. *Soviet Physics – Solid State.* 1967;9:523–524.
 40. de Bazelaire CM, Duhamel GD, Rofsky NM, Alsop DC. MR imaging relaxation times of abdominal and pelvic tissues measured in vivo at 3.0 T: preliminary results. *Radiology.* 2004;230:652–659.
 41. Gardener AG, Francis ST. Multislice perfusion of the kidneys using parallel imaging: image acquisition and analysis strategies. *Magn Reson Med.* 2010;63:1627–1636.
 42. Wu WC, Su MY, Chang CC, Tseng WY, Liu KL. Renal perfusion 3-T MR imaging: a comparative study of arterial spin labeling and dynamic contrast-enhanced techniques. *Radiology.* 2011;261:845–853.
 43. Rapacchi S, Smith RX, Wang Y, et al. Towards the identification of multi-parametric quantitative MRI biomarkers in lupus nephritis. *Magn Reson Imaging.* 2015;33:1066–1074.
 44. Santelli C, Nezafat R, Goddu B, et al. Respiratory bellows revisited for motion compensation: preliminary experience for cardiovascular MR. *Magn Reson Med.* 2011;65:1097–1102.
 45. Roberts DA, Detre JA, Bolinger L, et al. Renal perfusion in humans: MR imaging with spin tagging of arterial water. *Radiology.* 1995;196:281–286.
 46. Hoad CL, Cox EF, Gardener AG, Anblagan D, Francis ST. Multiphase True-FISP ASL in the kidney. In: *Presented at the 18th Annual Meeting International Society for Magnetic Resonance in Medicine.* Stockholm, Sweden: ISMRM; 2010:327.
 47. Riaz N, Shanker P, Wiersma R, et al. Predicting respiratory tumor motion with multi-dimensional adaptive filters and support vector regression. *Phys Med Biol.* 2009;54:5735–5748.
 48. Ruan D, Fessler JA, Balter JM, Keall PJ. Real-time profiling of respiratory motion: baseline drift, frequency variation and fundamental pattern change. *Phys Med Biol.* 2009;54:4777–4792.
 49. Ruan D, Fessler JA, Balter JM. Real-time prediction of respiratory motion based on local regression methods. *Phys Med Biol.* 2007;52:7137–7152.
 50. Spincemaille P, Nguyen TD, Prince MR, Wang Y. Kalman filtering for real-time navigator processing. *Magn Reson Med.* 2008;60:158–168.
 51. Ruan D. Kernel density estimation-based real-time prediction for respiratory motion. *Phys Med Biol.* 2010;55:1311–1326.
 52. Lee SJ, Motai Y. *Prediction and Classification of Respiratory Motion.* Heidelberg: Springer; 2014.
 53. Riviere CN, Thakral A, Iordachita II, Mitroi G, Stoianovici D. Predicting respiratory motion for active canceling during percutaneous needle insertion. In: *Presented at the 23rd Annual EMBS International Conference.* Istanbul, Turkey: IEEE; 2001:3477–3480.
 54. Wu H, et al. Statistical analysis and correlation discovery of tumor respiratory motion. *Phys Med Biol.* 2007;52:4761–4774.
 55. Putra D, Haas OC, Mills JA, Burnham KJ. A multiple model approach to respiratory motion prediction for real-time IGRT. *Phys Med Biol.* 2008;53:1651–1663.
 56. Hammon M, Janka R, Siegl C, et al. Reproducibility of kidney perfusion measurements with arterial spin labeling at 1.5 tesla MRI combined with semiautomatic segmentation for differential cortical and medullary assessment. *Medicine (Baltimore).* 2016;95:e3083.
 57. Gillis KA, McComb C, Foster JE, et al. Inter-study reproducibility of arterial spin labelling magnetic resonance imaging for measurement of renal perfusion in healthy volunteers at 3 Tesla. *BMC Nephrol.* 2014;15:23.
 58. Maleki N, Dai W, Alsop DC. Optimization of background suppression for arterial spin labeling perfusion imaging. *MAGMA.* 2012;25:127–133.
 59. Zhao F, Deng M, Yuan J, Teng GJ, Ahuja AT, Wang YX. Experimental evaluation of accelerated T1rho relaxation quantification in human liver using limited spin-lock times. *Korean J Radiol.* 2012;13:736–742.
 60. Wang WJ, Pui MH, Guo Y, Wang LQ, Wang HJ, Liu M. 3T magnetic resonance diffusion tensor imaging in chronic kidney disease. *Abdom Imaging.* 2014;39:770–775.